

Thermal shock resistant composite cathode material $\text{Sm}_{0.5}\text{Sr}_{0.5}\text{CoO}_{3-\delta}\text{-La}_{0.6}\text{Sr}_{0.4}\text{FeO}_{3-\delta}$ for solid oxide fuel cells

Maciej Tatko¹ · Michał Mosialek¹ · Aneta Kędra¹ · Elżbieta Bielańska¹ · Małgorzata Ruggiero-Mikołajczyk¹ · Paweł Nowak¹

Received: 20 June 2015 / Revised: 30 July 2015 / Accepted: 4 August 2015 / Published online: 21 August 2015
© The Author(s) 2015. This article is published with open access at Springerlink.com

Abstract The $\text{Sm}_{0.5}\text{Sr}_{0.5}\text{CoO}_{3-\delta}\text{-La}_{0.6}\text{Sr}_{0.4}\text{FeO}_{3-\delta}$ 1:1 composite, obtained by sintering mixture of components, was tested as a prospective cathode material for the oxygen reduction reaction in solid oxide fuel cells. Catalytic activity of the prepared material was characterized using electrochemical impedance spectroscopy at 400, 450, 500, 550, 600, 650, and 700 °C in oxygen and oxygen-argon mixtures in half-cells with $\text{Sm}_{0.2}\text{Ce}_{0.8}\text{O}_{1.9}$ as the electrolyte. Relatively low activation energies (65.2, 66.9, and 56.3 kJ mol⁻¹ for $P_{\text{O}_2}/P = 1.0, 0.1,$ and $0.01,$ respectively) for the reaction polarization resistance were observed. The specific surface area and the pore distribution were measured by N₂ adsorption method. The non-localized density functional theory was used in the analysis of the porosity data. The activity of the prepared composite depended on the pore structure which, in turns, depends on the sintering temperature. The best results were obtained for the composite sintered at the temperature of 1000 °C, where significant decrease in porosity is observed. The series of 53 thermal cycles, consisting of heating to 750 °C and cooling to room temperature confirmed the stability of the composite.

Keywords Lanthanum strontium ferrite · Samarium strontium cobaltite · Solid oxide fuel cell · Composite cathode · Samaria-doped ceria · Electrochemical impedance spectroscopy

Introduction

During intentional or accidental shut-down events, the elements of high-temperature fuel cells undergo thermal shocks. So, the compatibility of thermal expansion coefficients (TECs) between the electrolyte and the electrode materials is a factor of extreme importance. When the cathode material shows TEC much higher than electrolyte, like in the case of samarium strontium cobaltite $\text{Sm}_{0.5}\text{Sr}_{0.5}\text{CoO}_{3-\delta}$ (SSC) and ceria-based electrolytes, the simple way to resolve the problem is the dilution of the cathode material with the electrolyte material. For example, the composites consisting of SSC and an electrolyte material [1–6] reveal lower TEC than SSC and low polarization resistances. In the case of the cathode materials showing low ionic conductivity, like lanthanum strontium manganite (LSM), the additional advantage of using the composite containing an electrolyte material is the increase in its ionic conductivity. That, however, does not concern SSC because SSC shows higher ionic conductivity than samaria-doped ceria (SDC) electrolyte [7, 8]. However, the addition of an electrolyte to SSC may cause the increase of polarization resistance [1]. So, in the case of SSC cathode material, the admixture used to decrease TEC need not be the electrolyte. The recently published works [9–12] described attempts to prepare composite cathode materials by adding to SSC a component other than an electrolyte material. However, Co_3O_4 used in [9, 10], LSCF used in [11], and BSCF used in [12] has excellent catalytic activity in the oxygen reduction reaction (ORR) but rather high TECs, comparable to SSC, so no improvement in the compatibility between TECs of the electrolyte and the cathode material was reported.

Incompatibility between TECs of the cathode and the electrolyte may be the reason of the deterioration of the cathode performance. Composites in the percolation range consist of two intertwined continuous phases [13–15]. If the continuity of the paths of either the electronic or the ionic conducting

✉ Paweł Nowak
ncnowak@cyfronet.pl

¹ Jerzy Haber Institute of Catalysis and Surface Chemistry PAS, Niezapominajek 8, 30–239 Kraków, Poland

particles is interrupted, the electrode performance decreases [15]. That problem was thoroughly discussed by Zhang and Xia [16].

In the previous article [17], we described new composite cathodic material $\text{Sm}_{0.5}\text{Sr}_{0.5}\text{CoO}_{3-\delta}\text{-La}_{0.6}\text{Sr}_{0.4}\text{FeO}_{3-\delta}$ (SSC–LSF) showing TEC compatible with the ceria-based electrolyte and good catalytic activity in ORR. Contrary to most composite cathodic materials described in the literature, SSC–LSF is composed of two materials both showing simultaneously electronic and ionic conductivities. In the case of SSC–LSF composite, the LSF phase has low TEC ($12.8 \times 10^{-6} \text{ K}^{-1}$) [17], similar to the SDC electrolyte ($12.5 \times 10^{-6} \text{ K}^{-1}$) [18, 19], whereas SSC phase has high TEC ($19.9 \times 10^{-6} \text{ K}^{-1}$) [17]. During fast temperature changes LSF, expanding or shrinking with the electrolyte should remain stable, whereas SSC may be subjected to cracking. In the examined SSC–LSF composite, the low TEC component (LSF) is also an electronic conductor, so the appearance of the micro-cracks in the SSC phase should not lead to the interruption of the electronic conduction paths. To check that assumption, we have conducted a series of 53 thermal shocks. The stability of the electrode was evaluated by measuring the impedance spectra. The influence of the sintering temperature on the morphology of the composite and its catalytic activity in ORR was investigated too.

Experimental

SSC was prepared from nitrate solution by Pechini method as described in [20] and used together with commercial LSF powder (Sigma-Aldrich, grain size $<0.5 \mu\text{m}$) in the preparation of composite cathodes. The morphology of starting materials can be compared with each other in SEM images in Fig. 1. Both materials consist of similar particles, $\sim 200 \text{ nm}$ in size, but SSC particles are better separated from each other than LSF ones, whereas LSF is more uniform. The surface of LSF is smooth—at the SSC surface, thin slabs of 30–50 nm in diameter and approximately 5 nm thick appear. Note that the volume fraction of those slabs is negligibly small, so they could not be identified by either XRD or EDS. Indeed, XRD patterns of the prepared samples of SSC showed exclusively the lines characteristic to the perovskite structure of SSC [17] and the EDS analysis showed only Sm, Sr, and Ce. Similar slabs were observed by Su et al. [21] as well as Scurtu et al. [22] in the case of SSC–SDC composite, prepared with the use of the same reagents.

Two identical electrodes, the working electrode and the reference electrode, were screen printed on the surface of the electrolyte disk in the form of circles (5 mm diameter) using the cathode paste prepared from SSC and LSF mixed in the weight ratios of 1:1 and the Ink Vehicle (Fuel Cell Materials USA) (see Fig. 5d in [23]). SDC electrolyte disks of 20 mm diameter and 1 mm thickness were prepared as described

elsewhere [24]. Because our goal was to study the durability of the cathode material to thermal shocks, the cathode was tentatively deposited on a thick electrolyte layer (much thicker than usually in the studies on fuel cells) to force the cathodic material to shrink and to expand parallel with the electrolyte.

The lanthanum strontium cobalt ferrite (LSCF) counter electrode was deposited on the rear side of the electrolyte disk by screen printing of the LSCF paste (Fuel Cell Materials, USA) as detailed described in [17]. Then the pellet was dried and sintered at 900, 950, 1000, 1050, or 1100 °C for 2 h with heating and cooling rate $1.0 \text{ }^\circ\text{C min}^{-1}$. If not otherwise stated, cathodes sintered at 1000 °C were used in the measurements. The porous gold current collector layers were prepared by applying the gold paint Bright Gold Super M2D5 (Mennica Metale Szlachetne, Poland) on the top of these electrodes, drying and firing at 800 °C for 15 min with heating and cooling rate $1.5 \text{ }^\circ\text{C min}^{-1}$. Porous electrodes used in the experiments were 10 μm thick.

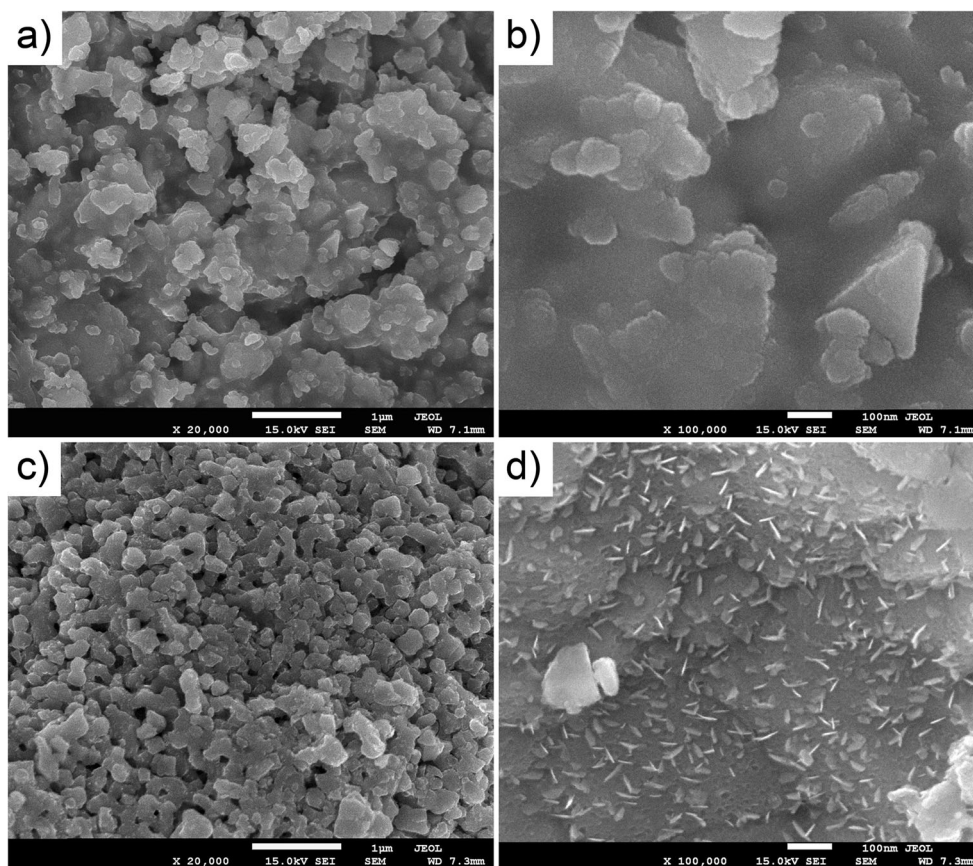
Thicker (1 mm) SSC–LSF electrodes were prepared the same way as the other ones for the porosity measurement. The thick composite cathode layer was separated from the electrolyte. The specific surface area and the porosity were measured by N_2 adsorption method with Quantachrome Autosorb–1 apparatus; the analysis of porosity data was based on the non-localized density functional theory (NLDFT). Before the measurement, the sample was degassed at 150 °C for 18 h under vacuum (ca. 10^{-6} Torr) and the N_2 adsorption was performed at $-195.8 \text{ }^\circ\text{C}$.

The microstructure observations were carried out by means of the scanning electron microscope (SEM) JEOL JSM–7500F with INCA PentaFetx3 EDS system.

The catalytic activity of the prepared composite electrodes was evaluated by measuring the polarization resistance connected with the ORR, using the electrochemical impedance spectroscopy (EIS). The measurements were conducted at different temperatures (400, 450, 500, 550, 600, 650, and 700 °C) at the atmospheric pressure, in pure oxygen or argon–oxygen mixtures (both Air Liquid Polska sp. z o. o.) at the oxygen relative pressures of 1.0, 0.1, and 0.01. The flow rate of the gas through the cell was 150 cm^3 per minute.

EIS measurements were performed using Gamry 300 series potentiostat/galvanostat/ZRA, in the three electrode setup. The frequency range used in EIS measurements was 0.01 to 300,000 Hz in the logarithmic frequency steps of ten points per decade. The amplitude of the sinusoidal voltage signal was 10 mV. The impedance spectra were registered at the spontaneously established potential. For the analysis of the impedance data, the Minuit [25] program, based on a complex non-linear regression least-square procedure, was used to fit the equation describing the assumed equivalent electrical circuit (EEC) to the measured data. More detailed description of the data-treatment procedure may be found in our previous publication [26].

Fig. 1 SEM images of starting materials: **a, b** LSF; **c, d** SSC



To make the interpretation of the EIS results easier, the current interruption method was used to estimate the ohmic part of the measured electrode impedance, connected with the resistance of the electrolyte, electrode material, cables, connections, etc. For that reason, the electrode was polarized applying constant cathodic potential bias of 10–100 mV (depending on temperature). When the current stabilized, its value was registered. The bias potential was selected to attain the stable current in the range of 0.1–0.5 mA cm⁻². Then the electrode was polarized with constant current equal to the previously registered. When the potential of the electrode stabilized, the circuit was opened and the overpotential decay was registered. Linear part of the potential time plot just at the beginning was considered to be the potential drop on the ohmic part of the circuit, and the resistance was calculated as the ratio of that potential drop to the current at the moment of the circuit opening.

Results

Electrochemical impedance spectroscopy

The examples of registered impedance spectra are shown in Fig. 2. Shapes of the impedance spectra were more and more

complicated for lower and lower temperatures, similarly as described by Nielsen and Hjelm [27] in the case of LSM–Zr_{1-x}Y_xO_{2-0.5x} composite electrodes. Electrical equivalent circuits (EECs) consisting of a resistor R₀ and several parallel resistor-and-capacitor pairs (R_i, C_i) connected in series were used to fit the measured impedance spectra. Each pair can reflect at least one slow step of the electrode process. Instead of capacitors, constant phase elements (CPEs) similarly as in many other papers [28–33] were used. The impedance of the CPE may be expressed by the following formula [33]:

$$Z_{\text{CPE}} = \frac{1}{2\pi f_0 C_0} \left(\frac{f_0}{jf} \right)^\alpha \quad (1)$$

where f is the frequency, f_0 is the frequency of reference, C_0 is the capacitance at the frequency of reference, and α is a coefficient close to 1 for an ideal capacitor, usually assuming a value between 0.7–1.0 in the case of non-ideal capacitance and close to 0.5 for diffusional impedance. In our case the frequency of reference was assumed to be 1000 Hz.

The shapes, and consequently the respective (R_i, CPE_i) pairs, were numbered in such a way that higher “i” means lower frequency. As many as five (R, CPE) elements and R₀ were used in some cases to obtain the good fit. Almost all spectra recorded at 700 °C consisted of three distinguishable depressed semicircles only (marked with the numbers 1, 4,

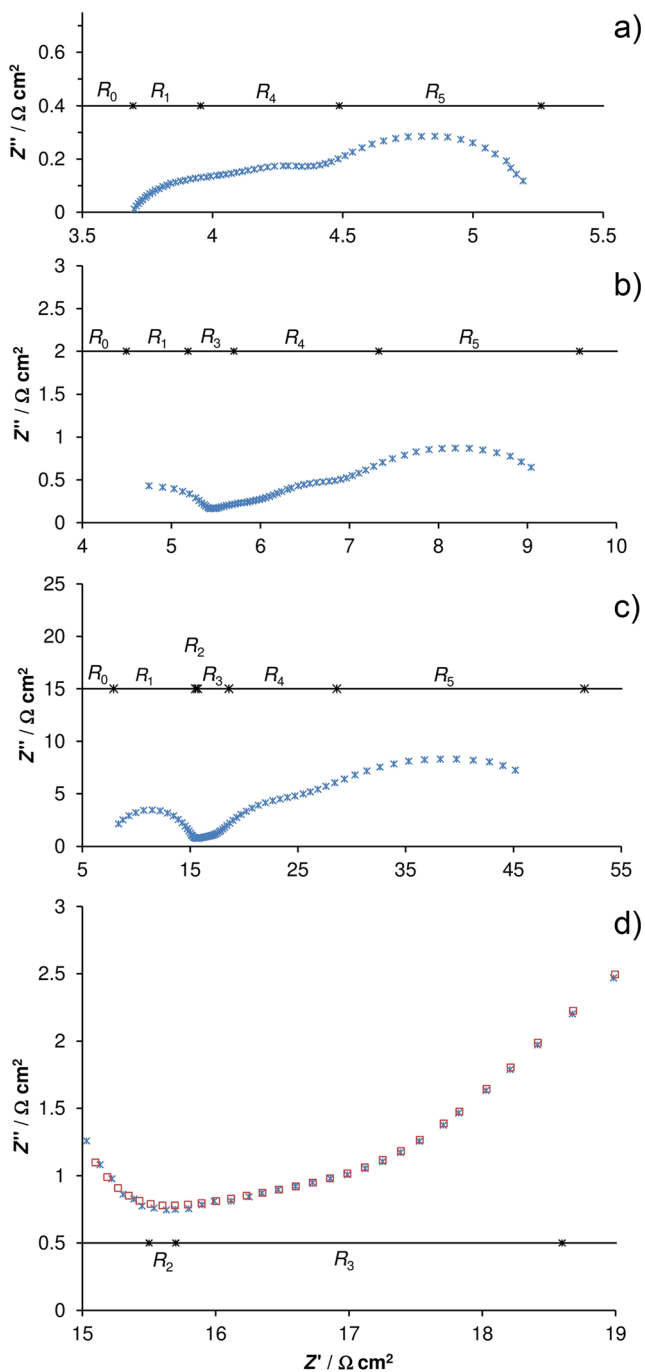


Fig. 2 Examples of EIS spectra in the Nyquist representation, recorded at different temperatures: **a** 700 °C, **b** 650 °C, **c** 550 °C, and **d** magnification of the part of (c) presenting the separation between the semicircles (R_2 , CPE₂) and (R_3 , CPE₃). In **d** the fitted values of impedance are also showed as empty squares

and 5), whereas spectra recorded at lower temperatures were fitted using EECs composed of either four (R, CPE) pairs (marked with the numbers 1, 3, 4, and 5) or five (R, CPE) pairs, depending on the number of distinguishable depressed semicircles.

Obtained resistances vary with oxygen concentration (Fig. 3). The dependence of the resistance R_1 related to the

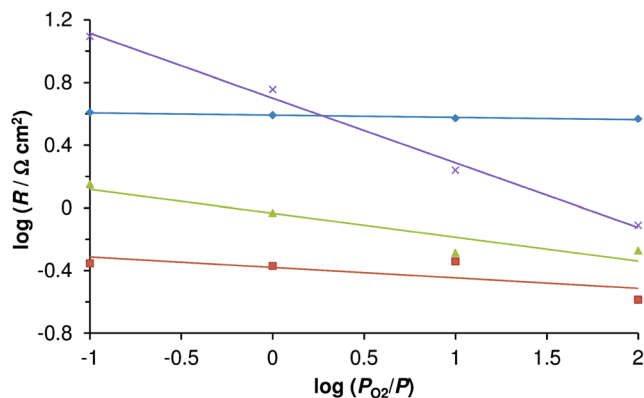


Fig. 3 Polarization resistance versus oxygen partial pressure at 700 °C

i th depressed semicircle on the oxygen concentration may be expressed by the formula:

$$\log(R_i) = a - m \log(P_{O_2}) \tag{2}$$

where a and m are coefficients. The value of m can be used for the identification of the type of a corresponding process [17, 28, 31, 34]. The m coefficients for R_0 , R_1 , R_3 are 0.00 ± 0.02 (see Table 1) which means that these resistances are oxygen concentration independent, hence they may represent ionic transfer of oxide ions across the electrolyte | electrode interface [28, 35], the transport of oxygen vacancies at the interface from the electrolyte side to the electrode [35], transport of oxygen ions through the electrolyte, and the resistances of interconnectors and cables. Moreover, these resistances are connected in parallel to very low capacitances C_1 , C_2 , C_3 . For example at 700 °C in pure oxygen, $C_1 = 1.6 \times 10^{-8}$, $C_2 = 2.7 \times 10^{-7}$, and $C_3 = 4.3 \times 10^{-6}$ F cm⁻². The origin of those capacitances may be the grain boundaries, but not only. In the case of solid electrolytes, only purely electronic conductivity manifests itself in the impedance spectrum as a simple resistor. In the case of either pure ionic or mixed conductivity, the flow of AC current through the continuous phase leads to the appearance in the impedance spectrum of a semicircle or a semi-tear. That problem was deeply discussed, among the others, in the paper of Lai and Haile [36].

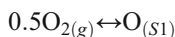
A sum of the resistances $R_0 + R_1 + R_2 + R_3$ called below ohmic resistance is not further analyzed. For R_2 m was not

Table 1 Coefficient m (formula 2) for different depressed semicircles in the impedance spectrum at different temperatures

| | 700 °C | 650 °C | 600 °C | 550 °C |
|-------|---------|--------|---------|---------|
| R_0 | 0.014 | 0.01 | 0.0037 | -0.0021 |
| R_1 | -0.0061 | -0.018 | -0.0084 | -0.014 |
| R_3 | - | 0.0007 | 0.023 | 0.0046 |
| R_4 | 0.15 | 0.005 | 0.13 | 0.1 |
| R_5 | 0.41 | 0.36 | 0.28 | 0.29 |

presented because R_2 attained very low values (see Fig. 2d) and was charged with a large relative error. The correctness of the interpretation of the sum $R_0 + R_1 + R_2 + R_3$ as the ohmic part of the electrode impedance was confirmed by comparing it to the ohmic resistance estimated by the current interruption method (see Fig. 4).

The interesting case is R_5 . Coefficient m for this resistance at 700 °C is close to 0.5 which can be considered to correspond to a surface diffusion step [31], but the corresponding shape in the impedance spectra is a symmetrical depressed semicircle which is not characteristic for either space-limited Warburg, Gerisher, Adler-Lane-Steele model [37], or porous electrode theory [27] impedances. The exponent α (Eq. 1) in the expression for the impedance of CPE_5 , equal to $0.68 \div 0.90$, was much higher than 0.5 expected for diffusion. According to Wang et al. [35], this semicircle represents dissociative adsorption of oxygen molecule



where s1 is the reaction site at the electrode surface. This assumption is also in accordance with the model of electrode reaction described for SSC point electrodes by Baumann et al. [38] and Grolig et al. [39]. According to these authors R_5 represents resistance connected to the surface oxygen exchange reaction and C_5 chemical capacitance related to oxygen stoichiometry changes in the bulk of the electrode. At lower temperatures, m connected with C_5 decreases to ~ 0.3 —similar slopes were presented by Fukunaga et al. [40] for ionic conduction,

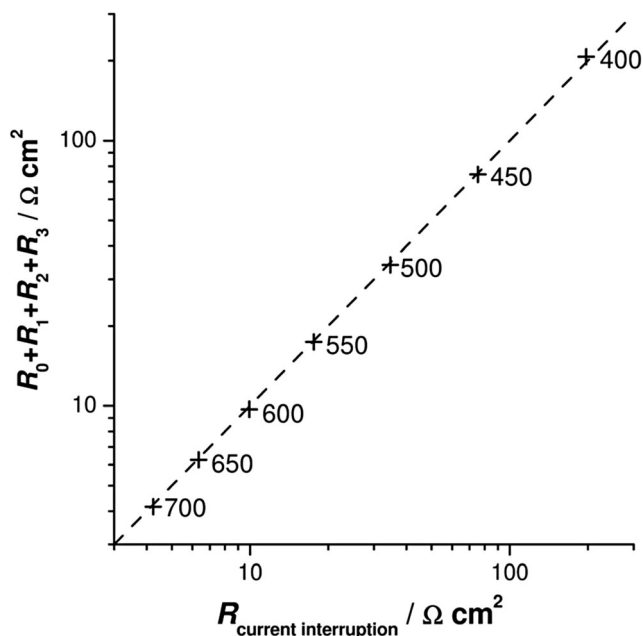


Fig. 4 The comparison between the ohmic part of the electrode impedance measured by the current interruption method and by EIS for the case of the measurement at 20 % O_2 and at different temperatures, marked at the points. The dashed line is a line traced at the angle of 45° and crossing the (0,0) point

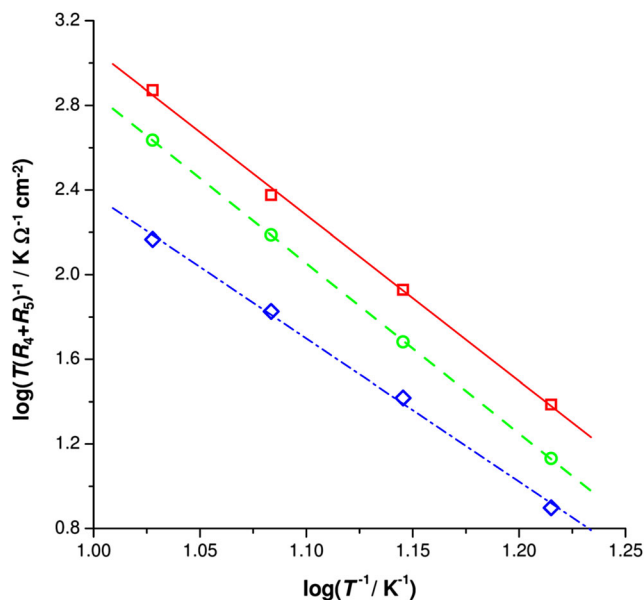
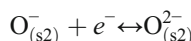


Fig. 5 Arrhenius plot of the electrode reaction resistance ($R_4 + R_5$)

adsorption, and desorption processes at dense SSC electrodes. Bauman et al. [38] reported chemical capacitances at 750 °C for SSC and LSF of 44 and 12 $mF\ cm^{-2}$ respectively, whereas we obtained the value of C_5 equal to 18 $mF\ cm^{-2}$ At 700 °C.

The coefficient m for R_4 revealed very weak dependence on the oxygen concentration ($0.05 < m < 0.15$). According to Wang [35], such value, close to 1/8, point to the transfer of the second electron.



where s2 is the site for the reaction at the electrode | electrolyte interface (another than s1). Philippeau et al. [28] proposed an explanation that m value is lower than 1/8 due to a mixed character of the process involving also the ionic transfer across the electrolyte-electrode interface.

The temperature dependence of a cathodic reaction resistance ($R_4 + R_5$) is plotted in Fig. 5. The activation energies are 65.2, 66.9, and 56.3 $kJ\ mol^{-1}$ for $P_{O_2}/P = 1.0, 0.1, \text{ and } 0.01$. The activation energies calculated for R_4 and R_5 separately

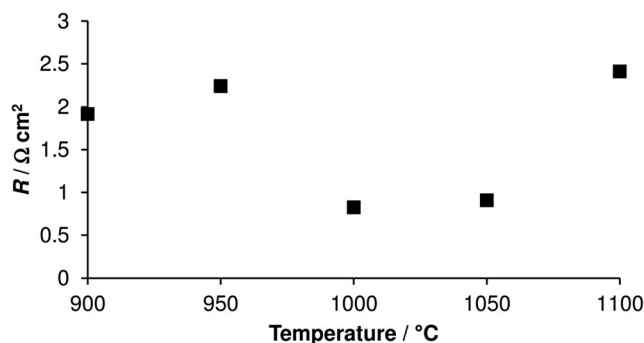


Fig. 6 Reaction resistance of composite cathodes sintered at different temperatures. Resistance measured at the temperature of 700 °C and at $P_{O_2}/P = 0.2$

(not showed) were similar to each other. The coefficient m for LSF electrodes given by Takeda et al. [41] is equal to 0.74 for both $\text{La}_{0.5}\text{Sr}_{0.5}\text{FeO}_{3-\delta}$ and $\text{La}_{0.7}\text{Sr}_{0.3}\text{FeO}_{3-\delta}$, whereas activation energies are 105 and 160 kJ mol^{-1} , respectively. The values measured in our case differ from those measured by Takeda et al. [41], so in our case, the reaction occurs mainly at the SSC surface, as may be expected. Activation energy of SSC electrode given by Park et al. [42] is 85.3 kJ mol^{-1} , which is much lower than that of LSF.

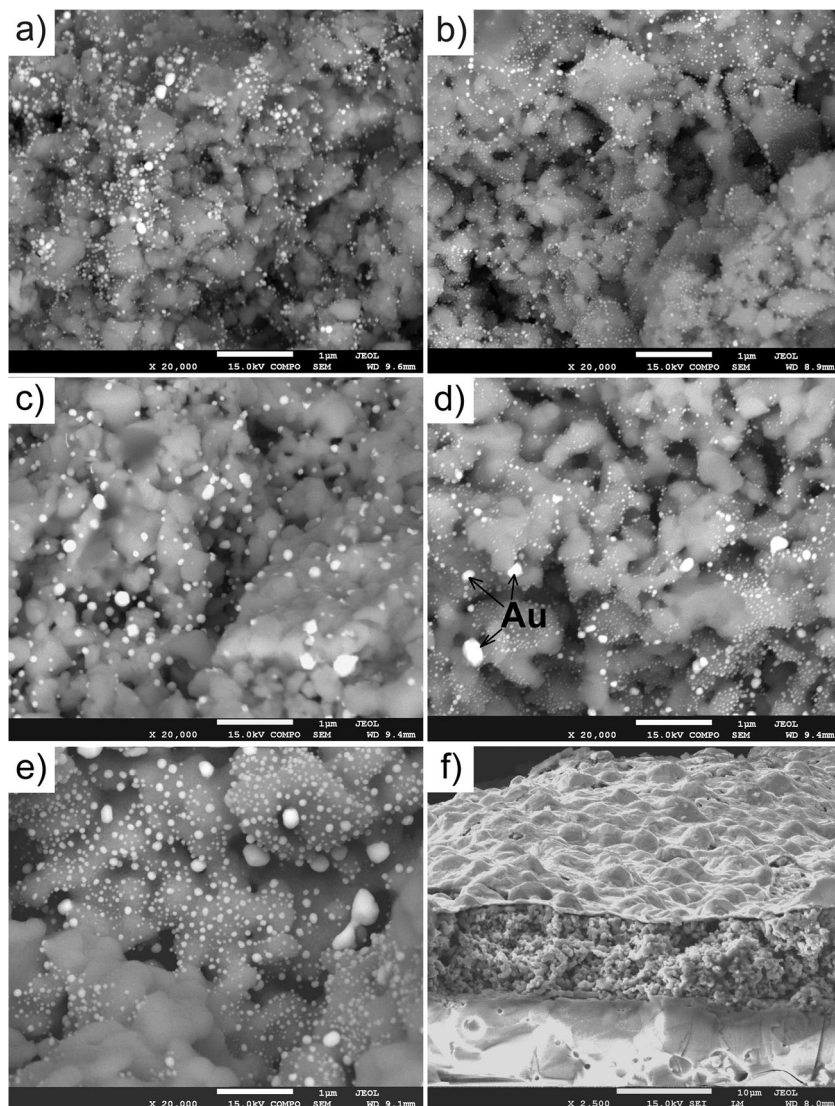
Influence of sintering temperature on the SSC–LSF composite cathode material properties

The polarization resistance obtained by fitting impedance spectra of the electrodes sintered at different temperatures and measured at the rest potential, 700 °C and $P_{\text{O}_2}/P = 0.2$, are presented in Fig. 6. It is to be seen that the polarization resistance depends on the sintering temperature, and the lowest polarization resistance

was obtained for cathode sintered at 1000 °C, only slightly higher at 1050 °C. So, if not otherwise stated, the cathodes sintered at 1000 °C were used in the experiments.

The microstructure of cathodes sintered at five different temperatures, after deposition of gold and after EIS measurements, is presented in Fig. 7. Cathodes sintered at 1050 and 1100 °C exhibited lower porosity and slightly melted edges of crystallites. It is interesting to observe that beside the top layer of the electrode, where continuous layer of gold current collector was deposited, small crystals of gold appeared in the bulk of the cathode, and that the amount of gold increases with the increasing sintering temperature. Gold was deposited at the surface of the cathode after sintering, at the same temperature for all samples (800 °C), also the impedance spectra were measured at the same temperature (700 °C), so the differences in the amount of gold reflects the differences in the morphology of the cathode material. As may be seen in Fig. 7, the samples sintered at the highest temperatures are built of

Fig. 7 SEM images of the SSC–LSF composite cathodes (cross sections) sintered at **a** 900 °C, **b** 950 °C, **c** 1000 °C, **d** 1050 °C, and **e** 1100 °C after the deposition of gold and EIS measurements. **f** The image of the cross section of the test half-cell sintered at 1100 °C. Bright particles are composed of gold, as confirmed by EDS analysis



bigger smoother particles, which facilitate the infiltration of gold into the cathode layer during the deposition. Fortunately, gold shows low catalytic activity in ORR [43, 44], so its presence should not influence the performance of the cathode.

The specific surface area of the composite cathode material measured by Multipoint BET method and microporosity parameters evaluated by the Monte Carlo differential pore volume distribution method were collected in Table 2. These measurements show that sintering at 1000 °C or higher temperatures leads to the closure of the micropores. Note that at the same time the polarization resistance decreases, which is most probably connected with the sintering of the grains with each other. However, the sample sintered at the temperature of 1100 °C shows again higher polarization resistance, most probably due to a significant decrease of the specific surface area and the closure of pores.

The pore-size distribution of the samples is presented in Fig. 8. The width of dominating pores in the region 0–50 nm is 2.5, 4.9, 4.9, 6.0, and 6.7 nm for cathodes sintered at 900, 950, 1000, 1050, and 1100 °C respectively. The macropores in the region 50–80 nm are well visible for samples sintered at 900 and 950 °C and reveal similar distribution. These pores start to disappear in the sample sintered at 1000 °C and disappear completely in the case of samples sintered at higher temperatures. The sample sintered at 1000 °C contains more mesopores than the other samples and practically no micropores. Dutta et al. [45] reported the influence of sintering temperature on density. These authors showed that the density of La_{0.8}Sr_{0.2}FeO₃ sintered at 900 and 950 °C was ~50 % of the theoretical density, whereas the density of samples sintered at higher temperatures was higher attaining ~90 % for the temperatures 1000 and 1050 °C and ~100 % at 1100 °C.

Stability of the SSC–LSF cathode

Polarization stability test

Polarization of the electrode may cause the occurrence of the side reactions proceeding with the participation of the electrode material leading to, for example, segregation of cations, change of the valence of cations, migration of the electrode material, or amelioration/deterioration of the contact between the electrode and the electrolyte [46–48]. Those changes are usually

Table 2 Specific surface area, micropore volume, and micropore surface area of samples sintered at different temperatures. Data obtained using the cathode material prepared in the form of thick (1 mm) layer

| Temperature/°C | 900 | 950 | 1000 | 1050 | 1100 |
|---|----------------------|----------------------|------|------|------|
| Specific surface area/m ² g ⁻¹ | 2.73 | 1.63 | 1.33 | 0.84 | 0.21 |
| Surface area of micropores/m ² g ⁻¹ | 0.74 | 0.51 | 0 | 0 | 0 |
| Volume of micropores/cm ³ g ⁻¹ | 4 × 10 ⁻⁴ | 3 × 10 ⁻⁴ | 0 | 0 | 0 |

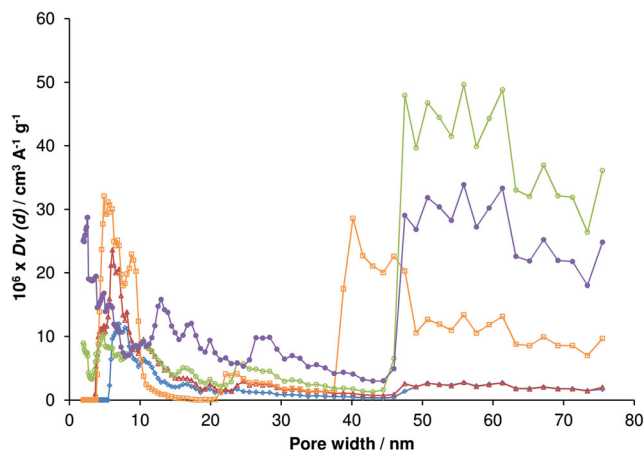


Fig. 8 Pore size distribution (NLDFT method) of samples sintered at 900 °C (dark-blue closed circles), 950 °C (green empty circles), 1000 °C (orange empty squares), 1050 °C (brown empty triangles), and 1100 °C (blue closed diamonds). Data obtained using the cathode material prepared in the form of thick (1 mm) layer

accompanied with the changes in the current measured at the constant polarization, especially in the initial period. Current recorded during 72 h stability test of SSC–LSF cathode under polarization at –0.5 V and 700 °C is presented in Fig. 9.

Only a 2 mA decrease in absolute value of current is observed during the initial 30 h. It means that no unfavorable phenomena, which might lead to the deterioration of the cathode performance, occurred at least during the first 30 h. That behavior is opposite to the trend reported by Gao et al. [4] for SSC–Ce_{0.85}Sm_{0.075}Nd_{0.075}O_{2-δ} (SNDC) composite, by Mosiałek et al. for BSCF [23], and by Wang and Jiang [49] for LSM.

Thermal shock tests

The test of 53 cycles of heating and cooling, simulating failures (due to either current interruption or uncontrolled rise in the temperature) was performed to check the resistance of the composite material to the thermal shocks. The single cycle consists of heating from 250 to 700 °C with the heating rate of 10 °C min⁻¹, EIS measurement, heating up to 750 °C with the heating rate of 10 °C min⁻¹, switching off the furnace, and cooling with initial

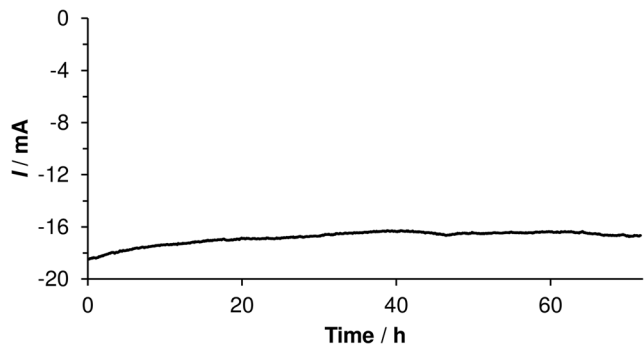


Fig. 9 Current recorded during constant polarization experiment at –0.5 V and 700 °C

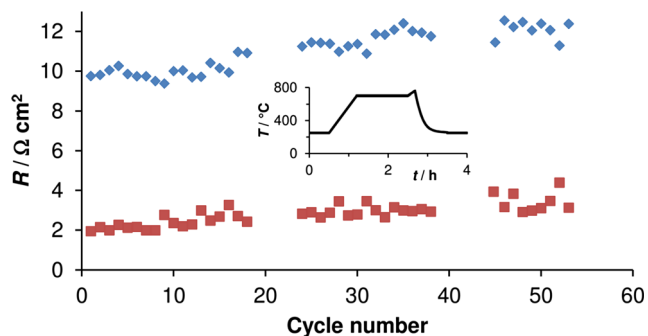


Fig. 10 Ohmic (blue diamonds) and reaction (red squares) resistances registered during consecutive 53 cycles of thermal shocks at 700 °C and at $P_{O_2}/P = 0.2$. Inset—scheme of the temperature changes in a single cycle during the test

rate of ~ 20 °C min^{-1} . Changes of ohmic and electrode reaction resistances measured during the test are presented in Fig. 10.

Small increase in both (ohmic and reaction) resistances observed during the test can be explained by the partial damage of the cathode structure, as presented in Fig. 11. The number of visible larger cracks on the cathode surface is comparable for fresh and cycled samples, whereas numerous smaller cracks appeared at the sample surface after the test.

Discussion

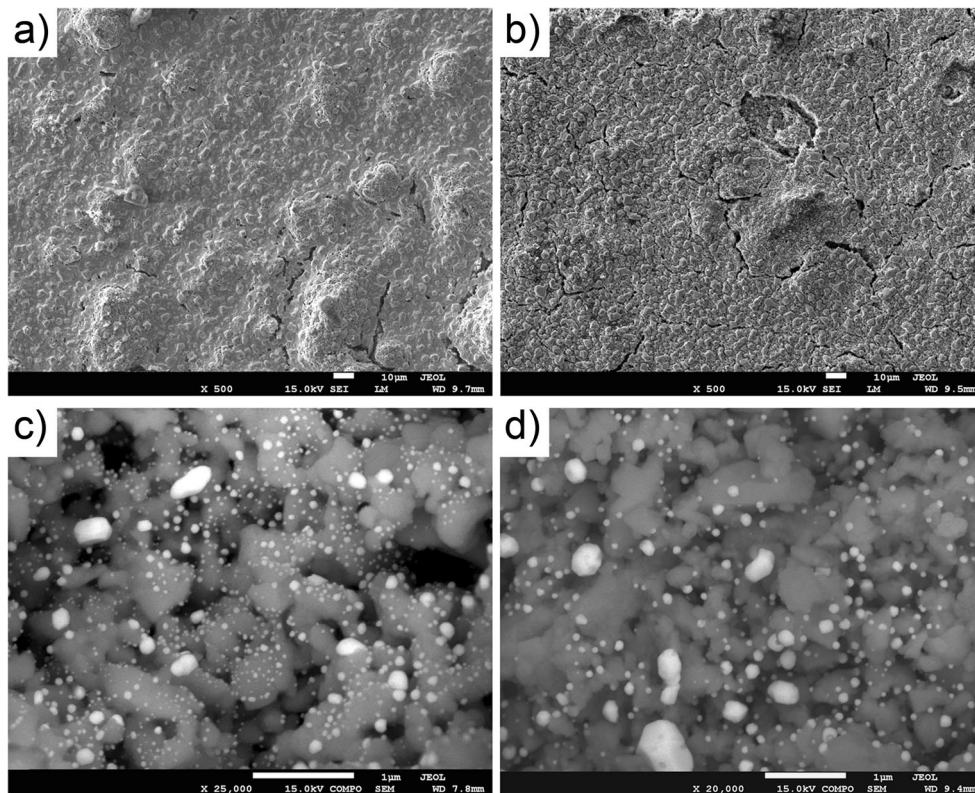
Originally, our intention was to prepare composite showing the value of TEC as close as possible to TEC of the electrolyte to

prevent the destruction of the electrolyte–cathode system during thermal changes. However, the best composite, from the point of view of its catalytic activity, was the composite containing SSC and LSF in the proportion 1:1 [17] which shows TEC still much higher than the electrolyte ($17.7 \times 10^{-6} \text{ K}^{-1}$ for composite versus 12.2 to $12.5 \times 10^{-6} \text{ K}^{-1}$ for SDC). Also, the difference in TECs between both components of the composite was relatively high ($12.8 \times 10^{-6} \text{ K}^{-1}$ for LSF and $19.9 \times 10^{-6} \text{ K}^{-1}$ for SSC). In spite of those relatively large differences in TECs, the cathode was stable and thermal shock resistant. In our opinion, cathode owes its stability to the fact that both the components of the composite show simultaneously electronic and ionic conductivity, contrary to most of the composite cathode materials, which usually consist of a material showing electronic conductivity and ionic conductivity as well as a material showing only ionic conductivity. So, in the examined case, the cracks in the structure of the catalytic material (in our case SSC) do not cause disruptions of electron conducting paths, preventing the elimination of the parts of cathode from the participation in ORR.

Conclusions

New promising cathode material for SOFCs, $\text{Sm}_{0.5}\text{Sr}_{0.5}\text{CoO}_{3-\delta}$ – $\text{La}_{0.6}\text{Sr}_{0.4}\text{FeO}_{3-\delta}$ (SSC–LSF) 1:1 composite, obtained by sintering mixture of components was characterized by SEM, BET, pore size distribution, and EIS methods. In spite of the still significant difference between TEC of the electrolyte and the

Fig. 11 SEM pictures of the composite SSC–LSF: **a, c** sample before the test and **b, d** sample after the test of 53 cycles; **a, b** top view and **c, d** cross section. The bigger hole in the center of the picture of the sample after the test (**b**) was not the result of the changes in temperature, but was unintentionally caused during dismounting



cathode material as well as between both components of the composite, the thermal shock test reveals only small impedance increase.

The best performance in oxygen reduction reaction (ORR) shows SSC–LSF obtained by sintering at 1000 °C which may be related to the pore structure of the composite. The macropores and micropores present at 900 and 950 °C start to disappear at 1000 °C; simultaneously, mesopores appear facilitating diffusion of oxygen.

ORR proceeds mainly at the surface of the SSC component of the composite, which shows much higher catalytic activity in ORR than the other component (LSF).

The impedance spectra measured in oxygen and argon–oxygen mixtures on the electrodes made of the investigated composite showed rather complicated shape, but two slow processes manifest itself in the form of depressed semicircles in the middle and low-frequency range. Those semicircles were ascribed to dissociative adsorption of oxygen at the cathode surface and the transfer of electron, respectively.

Acknowledgments The participation of Maciej Tatko in this work was financially supported by the EU Human Capital Operation Program, Polish Project No. POKL.04.0101–00–434/08–00.

Open Access This article is distributed under the terms of the Creative Commons Attribution 4.0 International License (<http://creativecommons.org/licenses/by/4.0/>), which permits unrestricted use, distribution, and reproduction in any medium, provided you give appropriate credit to the original author(s) and the source, provide a link to the Creative Commons license, and indicate if changes were made.

References

- Baek S-W, Bae J, Yoo Y-S (2009) *J Power Sources* 193:431–440
- Wang S, Zou Y (2006) *Electrochim Commun* 8:927–931
- Wang S, Zhong H (2007) *J Power Sources* 165:58–64
- Gao Z, Liu X, Bergman B, Zhao Z (2011) *J Power Sources* 196:9195–9203
- Park YM, Kim H (2012) *Int J Hydrog Energy* 37:15320–15333
- Wang F, Chen D, Shao Z (2012) *J Power Sources* 216:208–215
- Patakangas J, Ma Y, Jing Y, Lund P (2014) *J Power Sources* 263:315–331
- Yeh TC, Routbort JL, Mason TO (2013) *Solid State Ionics* 232:138–143
- Zhang H, Liu H, Cong Y, Yang W (2008) *J Power Sources* 185:129–135
- Zhang H, Yang W (2007) *Chem Commun* 41:4215–4217
- Lou X, Wang S, Liu Z, Yang L, Liu M (2009) *Solid State Ionics* 180:1285–1289
- Zhu W, Lu Z, Li S, Wei B, Miao J, Huang X, Chen K, Ai N, Su W (2008) *J Alloys Compd* 465:274–279
- Costamagna P, Costa P, Antonucci V (1998) *Electrochim Acta* 43:375–394
- Chen XJ, Chan SH, Khor KA (2004) *Electrochim Acta* 4:1851–1861
- Barbucci A, Bozzo R, Cerisola G, Costamagna P (2002) *Electrochim Acta* 47:2183–2188
- Zhang Y, Xia C (2010) *J Power Sources* 195:6611–6618
- Tatko M, Mosialek M, Dudek M, Nowak P, Kędra A, Bielańska E (2015) *Solid State Ionics* 271:103–108
- Sun C, Hui R, Roller J (2010) *J Solid State Electrochem* 14:1125–1144
- Kharton VV, Marques FMB, Atkinson A (2004) *Solid State Ionics* 174:135–149
- Dudek M, Mosialek M, Mordarski G, Socha RP, Rapacz-Kmita A (2011) *Arch Metall Mater* 56:1249–1255
- Su F, Zhang Y, Ni M, Xia C (2014) *Int J Hydrog Energy* 39:2685–2691
- Scurtu R, Somacescu S, Calderon-Moreno JM, Culita D, Bulimestru I, Popa N, Gulea A, Osiceanu P (2014) *J Solid State Electrochem* 210:53–59
- Mosialek M, Dudek M, Michna A, Tatko M, Kędra A, Zimowska M (2014) *J Solid State Electrochem* 18:3011–3021
- Mosialek M, Dudek M, Wojewoda-Budka J (2013) *Arch Metall Mater* 58:275–281
- James F, Roos M (1975) *Comput Phys Commun* 10:343–367
- Mosialek M, Nowak P, Dudek M, Mordarski G (2014) *Electrochim Acta* 120:248–257
- Nielsen J, Hjelm J (2014) *Electrochim Acta* 115:31–45
- Philippeau B, Mauvy F, Nicolle C, Fourcade S, Grenier JC (2015) *J Solid State Electrochem* 19:871–882
- Park YM, Kim H (2012) *Int J Hydrog Energy* 37:15320–15333
- Escudero MJ, Aguadero A, Alonso JA, Daza L (2007) *J Electroanal Chem* 611:107–116
- Xu X, Cao C, Xia C, Peng D (2009) *Ceram Int* 35:2213–2218
- Chen XJ, Khor KA, Chan SH (2003) *J Power Sources* 123:17–25
- Simka W, Mosialek M, Nawrat G, Nowak P, Żak J, Szade J, Winiarski A, Maciej A, Szyk-Warszyńska L (2012) *Surf Coat Technol* 213:239–246
- Liu B, Zhang Y, Zhang L (2009) *Int J Hydrog Energy* 34:1008–1014
- Wang Y, Zhang L, Chen F, Xia C (2012) *Int J Hydrog Energy* 37:8582–8591
- Lai W, Haile SM (2005) *J Am Ceram Soc* 88:2979–2997
- Adler SB, Lane JA, Steele BCH (1996) *J Electrochem Soc* 143:3554–3564
- Baumann FS, Fleig J, Cristiani G, Stuhlhofer B, Habermeier H-U, Maier J (2007) *J Electrochem Soc* 154:B931–B941
- Grolig JG, Froitzheim J, Svensson J-E (2014) *J Power Sources* 248:1007–1013
- Fukunaga H, Koyama M, Takahashi N, Wen C, Yamada K (2000) *Solid State Ionics* 132:279–285
- Takeda Y, Kanno R, Noda M, Tomida Y, Yamamoto O (1987) *J Electrochem Soc* 134:2656–2661
- Park I, Choi J, Lee H, Shin D (2013) *Ceram Int* 39:5561–5569
- Tomczyk P, Żurek S, Mosialek M (2009) *J Electroceram* 23:25–36
- van Hassel BA, Boukamp BA, Burggraaf AJ (1991) *Solid State Ionics* 48:155–171
- Dutta A, Mukhopadhyay J, Basu RN (2009) *J Eur Ceram Soc* 29:2003–2011
- Yaremchenko AA, Brinkman B, Janssen R, Frade JR (2013) *Solid State Ionics* 247:248:86–93
- Zhu W, Lu Z, Li S, Wei B, Miao J, Huang X, Chen K, Ai N, Su W (2008) *J Alloys Compd* 465:274–279
- Song X, Lee S, Chen Y, Gerdes K (2015) *Solid State Ionics* 278:91–97
- Wang W, Jiang SP (2004) *J Solid State Electrochem* 8:914–922